

**Dependence of high-order-harmonic generation on dipole moment in SiO<sub>2</sub> crystals**Chao Yu,<sup>1</sup> Xirui Zhang,<sup>1</sup> Shicheng Jiang,<sup>1</sup> Xu Cao,<sup>1</sup> Guanglu Yuan,<sup>1</sup> Tong Wu,<sup>1</sup> Lihua Bai,<sup>2</sup> and Ruifeng Lu<sup>1,3,\*</sup><sup>1</sup>*Department of Applied Physics, Nanjing University of Science and Technology, Nanjing 210094, People's Republic of China*<sup>2</sup>*Department of Physics, Shanghai University, Shanghai 200444, People's Republic of China*<sup>3</sup>*State Key Laboratory of Molecular Reaction Dynamics, Dalian Institute of Chemical Physics, Chinese Academy of Sciences, Dalian 116023, People's Republic of China*

(Received 25 April 2016; published 26 July 2016)

High-order-harmonic generation in  $\alpha$ -quartz SiO<sub>2</sub> is theoretically investigated under a strong laser field by solving the extended semiconductor Bloch equations. The accurate band structures as well as dipole moments between different bands are obtained from state-of-the-art first-principles calculations. We find that the shapes of  $k$ -space-dependent dipole moments play an important role in harmonic generation. The calculated results show that harmonic conversion efficiency is significantly enhanced and the cutoff energy is distinctly increased when the dipole moments change greatly along a valley in the  $k$  direction in the solid. Based on that dependence on the dipole moment, we also show that symmetry groups greatly affect the harmonic spectra from the solid materials. Moreover, a two-color synthesized field is used to achieve a supercontinuum harmonic spectrum near the cutoff region, and isolated attosecond pulses can be obtained directly by filtering out the harmonic radiation. We hope the contribution presented in this work provides a useful reference for future studies on laser-crystal interactions.

DOI: [10.1103/PhysRevA.94.013846](https://doi.org/10.1103/PhysRevA.94.013846)**I. INTRODUCTION**

The interaction of intense laser fields with atoms and molecules reveals many interesting strong-field phenomena, such as above-threshold ionization [1], above-threshold dissociation [2], and high-order-harmonic generation (HHG) [3,4], etc. As one of the most prominent methods to generate isolated attosecond pulses, HHG has been extensively studied on gaseous media over several decades [5–10]. The HHG process for a single atom is well explained by the semiclassical three-step model [3]: First, the electron is ionized via tunneling toward the continuum, then it is accelerated by the laser field, and finally the electron recombines with the parent ion, releasing the excess kinetic energy.

Recently, experiments [11–17] have demonstrated that the interaction of intense lasers with solid materials offers a new way to get HHG. Ghimire *et al.* [11,12] performed an experiment in a mid-infrared (IR) field and considered the Bloch oscillation mechanism, in which electrons and holes are reflected at an edge of the Brillouin zone in a ZnO crystal, as the source of HHG. Subsequently, solid HHG experiments have also been accomplished in longer wavelengths towards a terahertz field [13,14]. It is found that intraband HHG is dominant in this wavelength regime. Very recently, Lu *et al.* [15] applied a subperiod optical synthesized field with bandwidths that covered the ultraviolet and near-infrared spectral regions to a silicon dioxide crystal and showed that coherent extreme ultraviolet radiation is emitted with photon energies about 40 eV. In their work, electron's anharmonic motion is used to explain the generation of a high-frequency component when the oscillation of electrons is driven by a field in a lattice. They also observed that the total photon yield of fused silica is higher than that of the noble gases. Almost at the same time, Vampa *et al.* [16] experimentally added a weak second-harmonic beam to study the emission

process and demonstrated that the interband current created by electron-hole recollision is the dominant mechanism of solid HHG for midinfrared driving pulses; they also innovatively provided an all-optical technique to reconstruct momentum-dependent band gaps [17]. In addition, Hohenleutner *et al.* [18] measured HHG in a bulk solid directly in the time domain with a strong electric field oscillating at terahertz frequencies. Their experiments show that the electronic tunneling interference among different bands can control the emission of ultrashort bursts of high-harmonic radiation by a crystal.

For understanding the mechanisms of HHG in solid-state materials, several theoretical models [19–37], such as the time-dependent Schrödinger equation [19–22], density matrix equations [23–25], extended semiconductor Bloch equations (SBEs) [26–30], etc., have been employed in past years. Theoretical studies also prove that the discovery of HHG in solids presents hope for obtaining compact solid-state attosecond sources [31–33]. Normally, two primary contributions (i.e., intraband current and interband polarization) result in solid HHG. Because harmonic emission is sensitive to high spatial components of the band structure [15], band dispersions of high accuracy are required for dynamic calculations. In addition, dipole moments between different bands are very important because they determine the interband transition process in solid HHG [38]. In most theoretical works,  $k$ -space-dependent dipole moments were determined from the first-order  $k \cdot p$  theory approximation [39].

In this paper, we theoretically study HHG in solids by solving two-band SBEs. In contrast to previous works, band structures and  $k$ -dependent dipole moments of target materials used in the SBEs are all accurately obtained from high-level first-principles calculations. We find that both the conversion efficiency and the cutoff energy of the harmonic spectrum are higher than those obtained in first-order  $k \cdot p$  theory. This can be rationally attributed to nonlinearly anharmonic interferences between interband-transited electrons and intraband-excited electrons. In particular, we investigate in detail the solid HHG of  $\alpha$ -quartz SiO<sub>2</sub> materials with different symmetry

\*rflu@njust.edu.cn

groups. The calculated results indicate that HHG in solids is sensitive to the shapes of the  $\mathbf{k}$ -dependent dipole moments. Furthermore, we utilize a two-color technique commonly used in gas-phase atomic HHG to control the harmonic emission in solids. It is remarkable that an isolated pulse of about 70 as can be obtained directly by properly selecting the wavelength of the controlling laser field.

## II. THEORETICAL MODEL

In this work, the theoretical method to study the interaction of strong lasers with SiO<sub>2</sub> crystals ( $\alpha$ -quartz structure) is based on the solution of two-band SBEs. Atomic units are used throughout the paper, unless stated otherwise. The orientation of the reciprocal lattice of SiO<sub>2</sub> is chosen so that  $\mathbf{x}||\Gamma$ - $M$ ,  $\mathbf{y}||\Gamma$ - $K$ , and  $\mathbf{z}||\Gamma$ - $A$  (optical axis). We consider a linearly polarized laser field propagating through the crystal along the optical axis. The SBEs for describing the laser-crystal interaction with laser polarization along the  $\Gamma$ - $M$  direction read [27]

$$i \frac{\partial}{\partial t} p_k = \left( \varepsilon_c(k) - \varepsilon_v(k) - i \frac{1}{T_2} \right) p_k + (f_k^c - f_k^v) d(k) E(t) + i E(t) \nabla_k p_k, \quad (1)$$

$$\frac{\partial}{\partial t} f_k^{c(v)} = -2 \text{Im}[d(k) E(t) p_k^*] + E(t) \nabla_k f_k^{c(v)}. \quad (2)$$

Here,  $f_k^c$  and  $f_k^v$  are the populations of the lowest conduction band and the highest valence band, respectively. We assume that electrons are initially filled into the valence band.  $p_k$  is the microscopic interband polarization between the conduction and valence bands.  $T_2$  is the dephasing time.  $\varepsilon_c(k)$  and  $\varepsilon_v(k)$  are the  $\mathbf{k}$ -dependent energy bands of the lowest conduction band and the highest valence band, respectively, which are obtained from first-principles calculations using the VASP software (Appendix A) and fitted with the function  $\varepsilon_n(k) = \sum_{i=0}^{\infty} \alpha_n(i) \cos(ika)$  (Appendix B, Table I and Table II).  $a$  is the lattice constant along the  $\Gamma$ - $M$  direction which is set as 7.917 a.u. and 8.042 a.u. in SiO<sub>2</sub> structures with  $p3121$  and  $p3221$  symmetry groups, respectively.

Figure 1(a) shows the lowest conduction band and the highest valence band of SiO<sub>2</sub> with the  $p3121$  symmetry group along the  $\Gamma$ - $M$  direction. In Eqs. (1) and (2),  $d(k)$  is the dipole element, and  $E(t)$  is the temporal laser field. In most previous works, the employed  $d(k)$  are expressed in first-order  $\mathbf{k} \cdot \mathbf{p}$  theory as

$$d(k) = \frac{i d_0 [\varepsilon_c(0) - \varepsilon_v(0)]}{[\varepsilon_c(k) - \varepsilon_v(k)]}. \quad (3)$$

In our calculations, the  $\mathbf{k}$ -dependent dipole moments are obtained from

$$d(k) = \frac{i \langle \phi_c(k) | \hat{p} | \phi_v(k) \rangle}{[\varepsilon_c(k) - \varepsilon_v(k)]}, \quad (4)$$

where  $\phi_\lambda(k)$  is the normalized wave function of each  $\mathbf{k}$  point in a given band  $\lambda$ . Both cases of  $\mathbf{k}$ -dependent dipole moments above mentioned are shown in Fig. 1(b). In the first-order  $\mathbf{k} \cdot \mathbf{p}$  theory case, we set  $d_0 = 0.372$  to make a better comparison

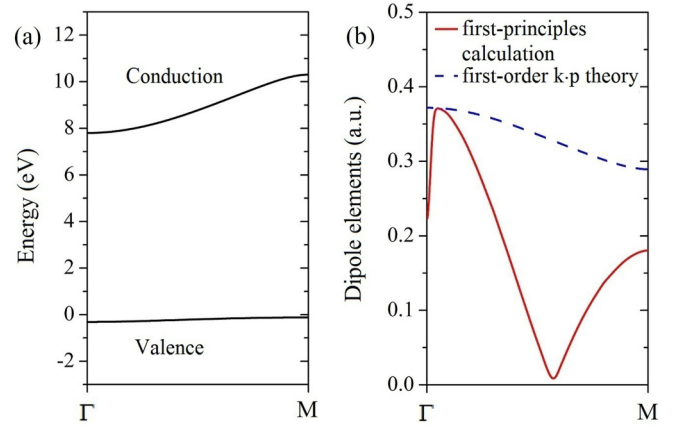


FIG. 1. (a) The lowest conduction band and highest valence band of SiO<sub>2</sub> with the  $p3121$  symmetry group along the  $\Gamma$ - $M$  direction. (b) The  $\mathbf{k}$ -dependent dipole moments calculated by first-principles theory (red solid line) and first-order  $\mathbf{k} \cdot \mathbf{p}$  theory (blue dashed line).

with the result calculated from high-level first principles. Obviously, the real dipole moment in the first-principles case changes more greatly along the  $\mathbf{k}$  direction than that in the first-order  $\mathbf{k} \cdot \mathbf{p}$  theory case.

Because of the motion of the carriers within the bands under a laser field, the intraband electric current  $J(t)$  and macroscopic interband polarization  $P(t)$  are given by

$$J(t) = \sum_{\lambda} \int_{\text{BZ}} v_k^{\lambda} f_k^{\lambda}(t) dk, \quad (5)$$

$$P(t) = \int_{\text{BZ}} [d(k) p_k(t) + \text{c.c.}] dk, \quad (6)$$

where  $v_k^{\lambda}$  is the group velocity generated from the derivative of the bands and  $\lambda$  is the band index. By Fourier-transforming the time-dependent intraband electric current  $J(t)$  and macroscopic interband polarization  $P(t)$ , the high-harmonic spectrum is calculated from

$$S(\omega) = \left| \frac{1}{\sqrt{2\pi}} \int_0^T \left[ J(t) + \frac{d}{dt} P(t) \right] e^{-i\omega t} dt \right|^2. \quad (7)$$

To investigate the temporal structures of solid HHG, we also perform time-frequency analyses by using the wavelet transformation of the total intraband current and interband polarization [40,41],

$$A(t, \omega) = \int \left( J(t') + \frac{d}{dt} P(t') \right) \sqrt{\omega} W(\omega(t' - t)) dt', \quad (8)$$

where  $W(\omega(t' - t))$  is the mother wavelet with the formula  $W(x) = (1/\sqrt{\tau}) e^{ix} e^{-x^2/2\tau^2}$ , and  $\tau = 10$  fs in our calculations. Finally, an attosecond pulse can be obtained by superposing the appropriate harmonics,

$$I(t) = \left| \sum_q \left( \int_0^t \left[ J(t') + \frac{d}{dt} P(t') \right] e^{-i\omega t'} dt' \right) e^{-iq\omega t} \right|^2, \quad (9)$$

where  $q$  is the harmonic order.

### III. RESULTS AND DISCUSSION

Figure 2(a) shows the high harmonic spectrum of SiO<sub>2</sub> with symmetry group *p3121* from different dipole elements in Fig. 1(b). The driving laser used here is a 6 fs/800 nm infrared laser field, which is plotted in Fig. 3(a). The laser peak intensity is  $I_1 = 5.0 \times 10^{12}$  W/cm<sup>2</sup> (about 0.6 V/Å), which is much lower than the damage threshold of SiO<sub>2</sub> under such a short pulse. We set the dephasing time as  $T_2 = 2.7$  fs which is equal to  $T_0/2$  ( $T_0$  is the optical cycle of the fundamental field). It is clear that the cutoff energy of the harmonic spectrum is distinctly extended with the real dipole element from first-principles calculations. In addition, the conversion efficiency of the harmonic is much higher than that in the first-order  $\mathbf{k} \cdot \mathbf{p}$  approximation case.

To better understand the emission process of solid HHG, the time-frequency analyses of HHG for the first-order  $\mathbf{k} \cdot \mathbf{p}$  theory case and the first-principles case are presented in Figs. 2(b) and 2(c), respectively. In gases, harmonics are emitted at different phases in the field near zero due to the time delay of the acceleration and recombination processes. In solids, however, we find that the harmonic is emitted at the field peak every half cycle, which is consistent with other theoretical work [25]. In contrast to the first-order  $\mathbf{k} \cdot \mathbf{p}$  theory case, the photon energy is increased at all peaks in the real first-principles case, as shown in Fig. 2(c). In fact, the real value of the dipole element is lower than that from the  $\mathbf{k} \cdot \mathbf{p}$  approximation [Fig. 1(b)]. Thus, the shapes of the  $\mathbf{k}$ -dependent dipole elements could be the key factors leading to the high-photon-energy emission, and it is reasonable that the extended high-energy harmonics mainly come from nonlinearly anharmonic interference between interband-transited electrons and intraband-excited electrons at the field peaks.

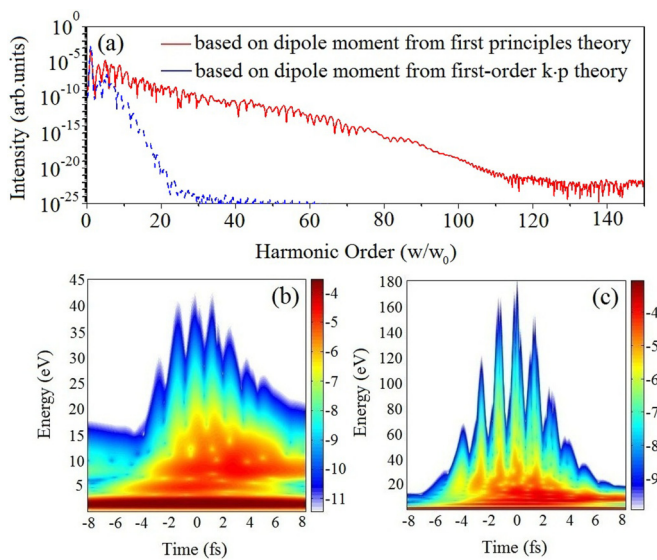


FIG. 2. (a) High-harmonic spectra of SiO<sub>2</sub> with the *p3121* symmetry group from dipole elements calculated by first-principles theory (red solid) and first-order  $\mathbf{k} \cdot \mathbf{p}$  theory (blue dashed). Time-frequency analyses of HHG based on dipole moments from (b) first-order  $\mathbf{k} \cdot \mathbf{p}$  theory and (c) real first-principles calculations.

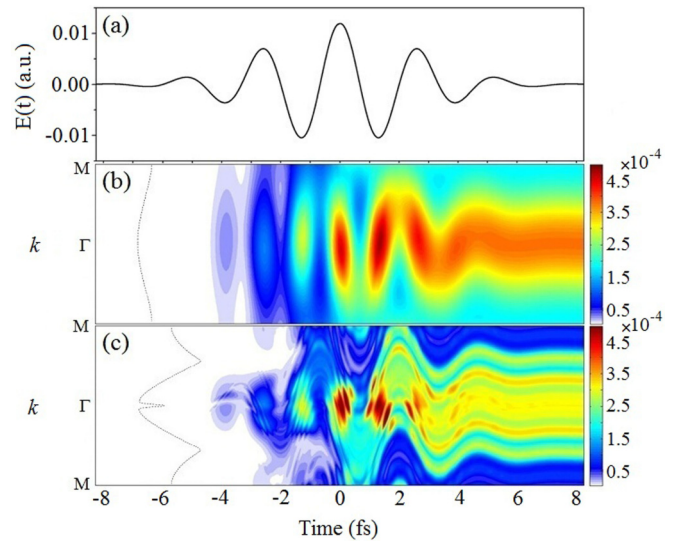


FIG. 3. (a) Electric field profile of a 6 fs/800 nm laser. Populations of conduction band for two cases based on dipole moments from (b) first-order  $\mathbf{k} \cdot \mathbf{p}$  theory and (c) real first-principles calculations.

In order to clearly address the physics of this process, the populations of the conduction band for two cases are shown in Figs. 3(b) and 3(c), respectively. Under the interaction with the laser field, electrons in the crystal are excited from the valence

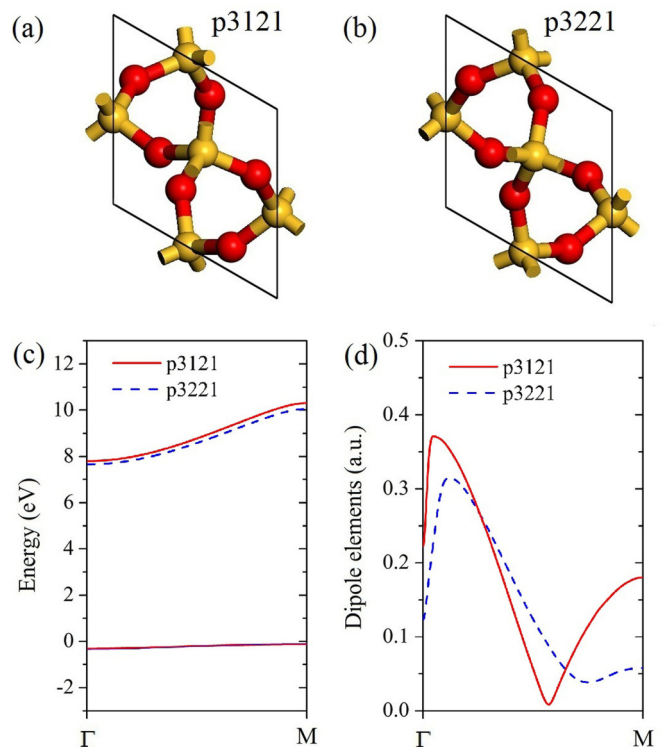


FIG. 4. The crystal structures of (a) *p3121* and (b) *p3221* symmetry groups by using real first-principles dipole element in the unit cell. (c) The band structures of conduction band and valence band along the  $\Gamma$ - $M$  direction with *p3121* (red solid) and *p3221* (blue dashed) symmetry groups. (d) The  $\mathbf{k}$ -dependent dipole moments of *p3121* (red solid) and *p3221* (blue dashed) SiO<sub>2</sub>.

to the conduction band at each peak of the field and oscillate in both bands. Undoubtedly, some of the excited electrons can also transit back to the valence band when the field is near zero. By contrast with the populations of the conduction band for the  $\mathbf{k} \cdot \mathbf{p}$  approximation case in Fig. 3(b), more interference structures can be found for the first-principles case in Fig. 3(c). This special phenomenon comes from the different shape of the dipole element. In the accurate first-principles case, the narrow valley of the dipole moment around the  $\Gamma$  point will lead to irregular excitation. This oscillated irregular electronic population results in nonlinearly anharmonic interference with the following excited electrons and generates photon with high energy.

Then, we investigate the HHG in  $\text{SiO}_2$  crystal with two different symmetry groups ( $p3121$  and  $p3221$ ) using first-principles dipole moments. Figures 4(a) and 4(b) show the crystal structures of these two symmetry groups in unit cell. It can be seen from the general structures that all lattice parameters are very similar between the two  $\text{SiO}_2$  crystals (Appendix A) and merely the symmetrical arrangements of the atoms are different. The corresponding band structures along the  $\Gamma$ - $M$  direction are shown in Fig. 4(c). Obviously, only tiny

differences exist between the conduction bands. However, the  $\mathbf{k}$ -dependent dipole moments for these two symmetry groups are quite different, as shown in Fig. 4(d).

In Fig. 5, we compare our theoretical results with available experimental data [15]. The laser fields used in experiments and the corresponding harmonic spectra are shown in Figs. 5(a) and 5(b). In order to avoid the singularity at the start of the laser fields obtained from the literature, we smooth the laser profiles in the first few femtoseconds [insets in Figs. 5(c)—5(f)]. By using first-principles dipole moments, we calculate the harmonic spectra for the  $\text{SiO}_2$  crystal with symmetry group  $p3121$  from few-cycle and half-cycle laser fields, as shown in Figs. 5(c) and 5(d), respectively. The same calculation results but for symmetry group  $p3221$  are provided in Figs. 5(e) and 5(f). For better comparison, the peak intensities of all the harmonic spectra are normalized to unity. In general, our calculations reproduce the main characteristics of the experimental measurements that discrete harmonics are generated and the harmonic spectra seem not sensitive to the CEP variation in few-cycle fields [Figs. 5(c) and 5(e)]. Moreover, the half-cycle-field wave form gives rise to EUV continua [Figs. 5(d) and 5(f)], and the amplitude and

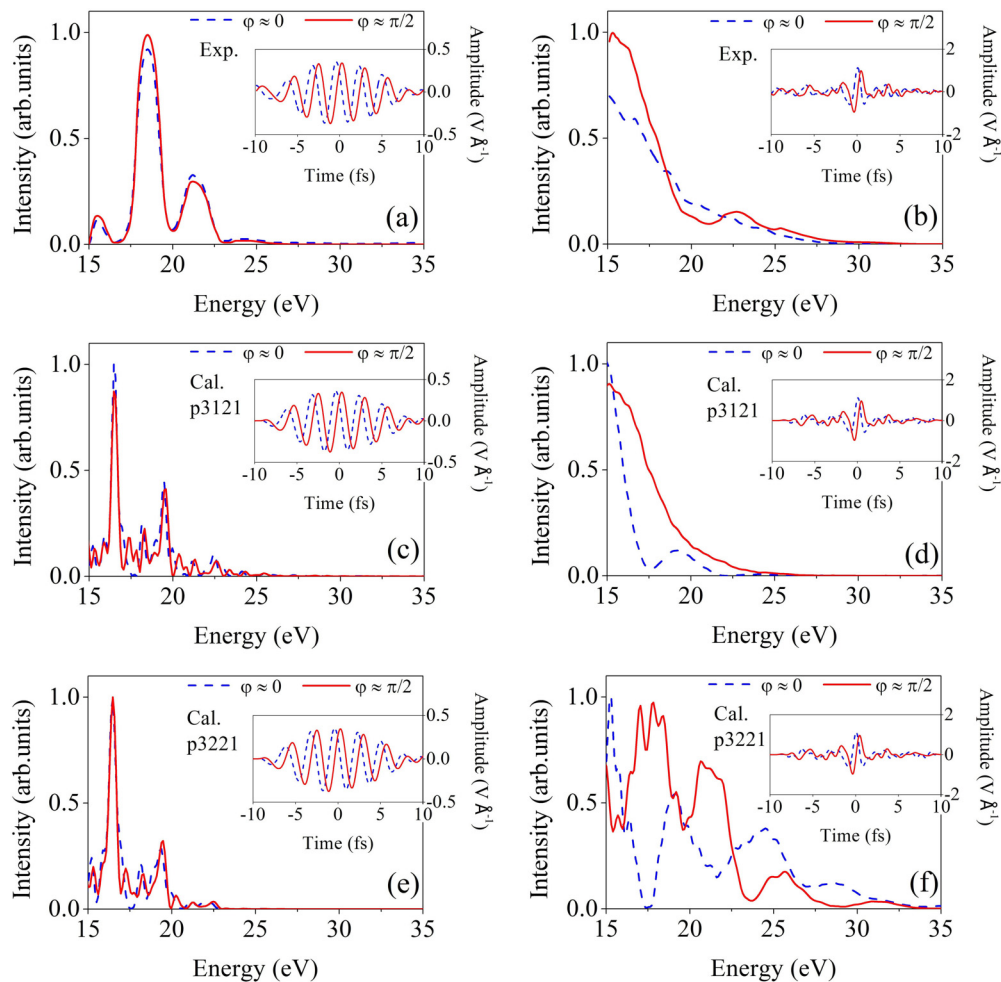


FIG. 5. (a) and (b) The experimental laser profiles and corresponding harmonic spectra from Figs. 3(a) and 3(d) in Ref. [15], respectively. The harmonic spectra with symmetry group  $p3121$  using first-principles dipole moments from a few-cycle laser field (c) and a half-cycle laser field (d). (e) and (f) are the same as (c) and (d) respectively but for symmetry group  $p3221$ . Here, the intensity of the harmonic spectrum  $I(\omega) = \omega^2 S(\omega)$  is used for better comparison with experimental data, and  $T_2 = 0.5$  fs.

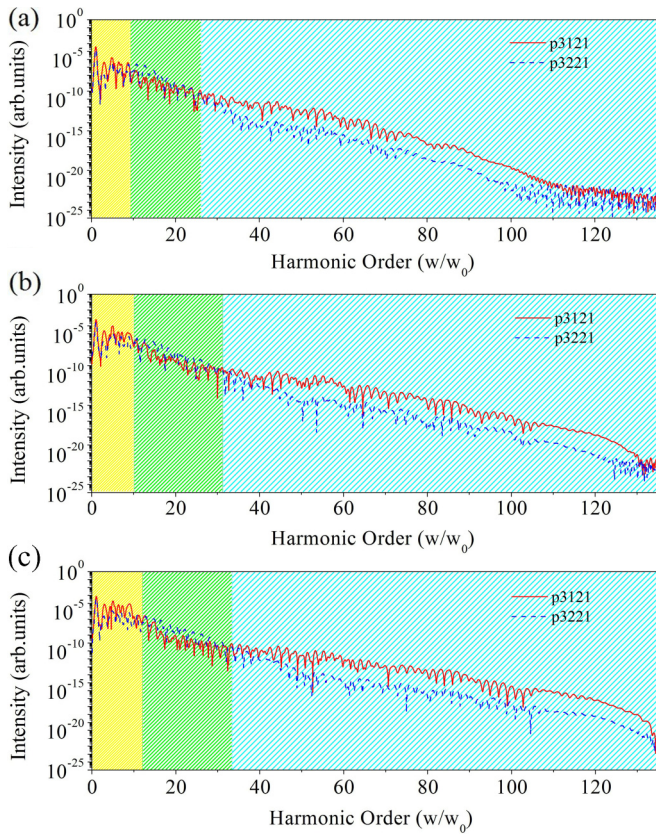


FIG. 6. HHG spectra generated from  $p3121$  (red solid) and  $p3221$  (blue dashed)  $\text{SiO}_2$  in laser fields with peak intensities of (a)  $5.0 \times 10^{12} \text{ W/cm}^2$ , (b)  $8.0 \times 10^{12} \text{ W/cm}^2$ , and (c)  $1.0 \times 10^{13} \text{ W/cm}^2$ .

shape show a considerable sensitivity to the CEP. Although the calculated peaks and cutoffs of all the harmonic spectra are lower than the experimental results in energy, this is understandable as the band gap of the  $\text{SiO}_2$  crystal from our first-principles calculations is about 1 eV lower than its experimental value. In addition, the shapes of the HHG peaks for symmetry groups  $p3121$  and  $p3221$  are very similar under the few-cycle field. However, in the half-cycle field, only the calculated HHG for symmetry group  $p3121$  agrees well with the experimental results.

Figures 6(a)–6(c) provide a comparison between the HHG spectra generated from  $p3121$  and  $p3221$   $\text{SiO}_2$  crystals interacting with lasers of peak intensities  $I = 5.0 \times 10^{12} \text{ W/cm}^2$ ,  $8.0 \times 10^{12} \text{ W/cm}^2$ , and  $1.0 \times 10^{13} \text{ W/cm}^2$ , respectively. As the peak intensity of the field increases, the cutoff energy of the harmonics is extended linearly for both  $p3121$  and  $p3221$  symmetries, in agreement with the findings in experiments [11,15]. In addition, we find that the conversion efficiency of the harmonic spectrum for the  $p3121$  group is higher than that of the  $p3221$  group in the low-energy region (yellow background) and the high-energy region (cyan dense diagonals) near the harmonic cutoff; this is especially evident in the high-energy region. However, the harmonic spectrum for the  $p3221$  group shows higher conversion efficiency in the middle energy region (green sparse diagonals). These findings indicate that the conversion efficiency of HHG can

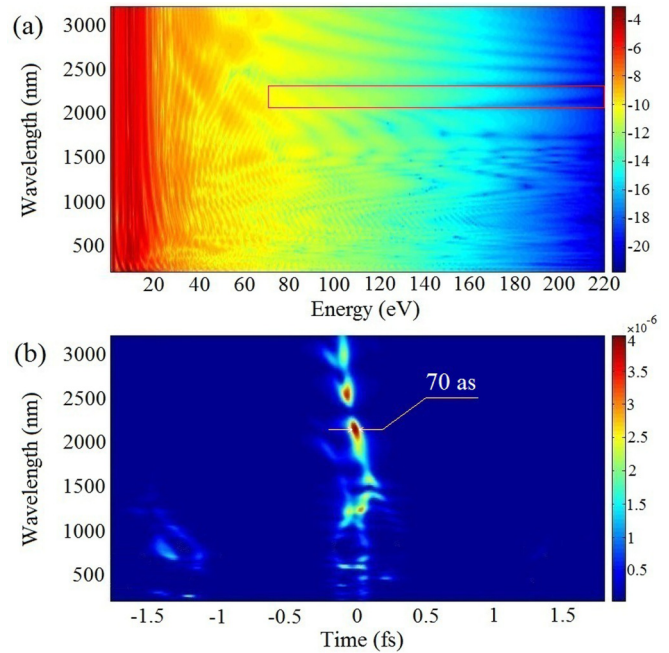


FIG. 7. (a) HHG spectra of  $\text{SiO}_2$  with  $p3121$  group in two-color synthesized laser field. The laser peak intensities corresponding to the fundamental field and controlling field are  $I_1 = 5.0 \times 10^{12} \text{ W/cm}^2$  and  $I_2 = 5.0 \times 10^{11} \text{ W/cm}^2$ , respectively. The wavelength of the fundamental field is 800 nm, and the wavelength of the controlling field changes from 200 to 3200 nm. (b) Attosecond pulses generated by directly filtering out harmonics below 70 eV as shown in (a).

be effectively enhanced by properly selecting the symmetry group of the crystals, which may provide a feasible way to develop attosecond optics in solid materials.

As is well known in gas HHG studies, adding a weak controlling field to a single driving laser field is usually an effective means to extend the harmonic cutoff and manipulate the quantum paths of the electron. Figure 7(a) provides the HHG spectra of  $\text{SiO}_2$  with the  $p3121$  symmetry group in a two-color synthesized laser field as

$$E(t) = E_1 f_1(t - t_0) \cos[\omega_1(t - t_0) + \varphi_1] + E_2 f_2(t - t_0) \cos[\omega_2(t - t_0) + \varphi_2]. \quad (10)$$

The laser peak intensities corresponding to  $E_1$  and  $E_2$  are  $I_1 = 5.0 \times 10^{12} \text{ W/cm}^2$  and  $I_2 = 5.0 \times 10^{11} \text{ W/cm}^2$ , respectively. A Gaussian envelope  $f(t - t_0)$  is taken and the full width at half maximum (FWHM) of both lasers is fixed at 6 fs. Here,  $t_0 = 11.55 \text{ fs}$ ,  $\omega_1$  is the frequency of the 800 nm fundamental field, and  $\omega_2$  is the frequency of the controlling field. We keep the carrier-envelope phases (CEPs) as  $\varphi_1 = \varphi_2 = 0$ . In the two-color scheme, the wavelength of the second weak field is used to control the harmonic emission. With the help of the second field, the maximal photon energy of the emitted harmonic can reach more than 200 eV. By changing the wavelength of the controlling field from 200 to 3200 nm, we get a supercontinuum harmonic spectrum, when the wavelength of the controlling field is larger than 2000 nm. In Fig. 7(b), by directly filtering out harmonics below 70 eV

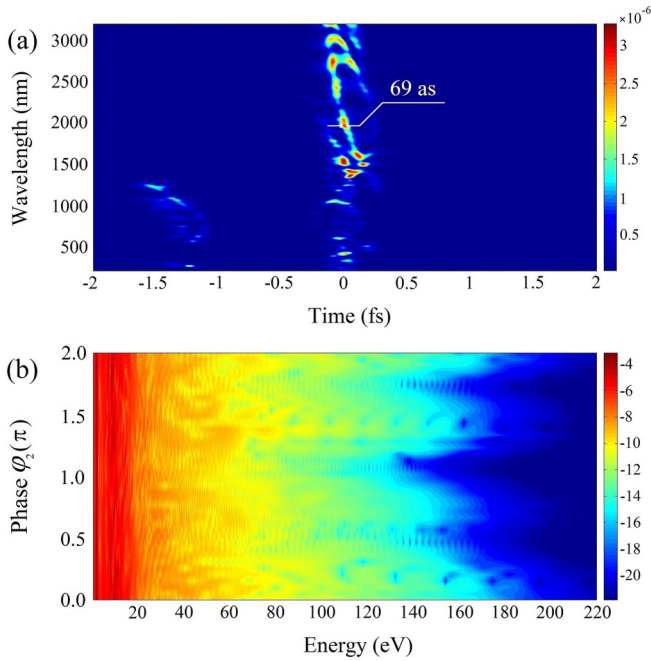


FIG. 8. (a) The wavelength-dependent attosecond emission spectrum for SiO<sub>2</sub> with  $p3121$  group in a two-color synthesized laser field. The laser parameters are identical to those in Fig. 7 but using a longer 15 fs controlling laser. (b)  $\varphi_2$ -dependent harmonic spectra with the wavelength of the controlling laser at 2000 nm. Other laser parameters are identical to those in (a).

in Fig. 7(a), the strongest isolated 70 as pulse can be generated at the wavelength of the controlling field, around 2150 nm.

To make the proposed scheme more feasible, we choose a longer controlling laser with the FWHM of 15 fs. The wavelength-dependent attosecond emission spectrum is shown in Fig. 8(a). We also find isolated attosecond pulses near the controlling wavelength of 2000 nm. Similarly, an isolated 69 as pulse is obtained at 1960 nm wavelength of the controlling field. In addition, we study the effect of the CEP of the controlling field ( $\varphi_2$ ) on the HHG in the two-color scheme. The phase-dependent harmonic spectra are shown in Fig. 8(b). The fundamental field is identical to that in Fig. 7. The peak intensity, FWHM, and wavelength of the controlling field are  $5.0 \times 10^{11}$  W/cm<sup>2</sup>, 15 fs, and 2000 nm, respectively. It is clear that the cutoff in the harmonic spectra reaches a higher energy when  $\varphi_2$  is close to zero. On the contrary, cutoff energy is decreased at  $\varphi_2$  near  $\pi$ .

#### IV. CONCLUSION

In summary, we theoretically explored the HHG in solids by solving the quantum SBEs. The dipole moment of the SiO<sub>2</sub> crystal is quite different between the first-order  $\mathbf{k} \cdot \mathbf{p}$  theory approximation and state-of-the-art first-principles calculations. By comparing the harmonic spectra from different  $\mathbf{k}$ -dependent dipole moments, we found that both the conversion efficiency and the cutoff energy of the harmonic spectrum are higher with more real dipole moments. Nonlinearly anharmonic interference between interband-transited electrons and intraband-excited electrons is responsible for this discrepancy

in HHG. Then, we investigated the HHG of SiO<sub>2</sub> crystals with different symmetry groups  $p3121$  and  $p3221$ . We also found that the harmonic conversion efficiency in the high-energy region for SiO<sub>2</sub> with symmetry group  $p3121$  is about two orders of magnitude higher than for the  $p3221$  SiO<sub>2</sub> crystal. Moreover, we used the two-color technique to control the harmonic emission in SiO<sub>2</sub> solid, and found that an isolated ultrapulse (tens of attoseconds) can be obtained at a wavelength of the controlling field around 2000 nm. In this emerging field, a lot of breakthroughs have been accomplished in both experimental measurements and theoretical analyses, which inspired us to deeply explore the fundamental physics behind the novel observations of solid-state harmonics. With the advances in laser technology, theoretical simulations should be carefully carried out, taking accurate dipole moments and the symmetry of sample crystals into account. Therefore, we expect that the findings in this study are not only meaningful for the SiO<sub>2</sub> studied here but also applicable for other materials, which will provide useful insights into the practical production of isolated attosecond pulses in solids.

#### ACKNOWLEDGMENTS

This work was supported by NSF of China (Grants No. 21373113 and No. 61275103), and the Fundamental Research Funds for the Central Universities of China (Grants No. 30920140111008 and No. 30916011105).

#### APPENDIX A: COMPUTATIONAL DETAILS OF FIRST-PRINCIPLES CALCULATIONS

All the first-principles calculations were performed using the Vienna *ab initio* simulation package (VASP) code [42–44]. Geometric optimizations of  $\alpha$ -quartz SiO<sub>2</sub> crystals with symmetry groups  $p3121$  and  $p3221$  were done within the generalized gradient approximation in the parametrization of Perdew, Burke, and Ernzerhof (PBE) [43]. The energy cutoff was set to be 550 eV. Geometry structures are fully relaxed until the convergence criteria of energy and force are less than  $10^{-5}$  eV and  $0.01 \text{ eV}\text{\AA}^{-1}$ , respectively. A Monkhorst-Pack mesh of  $11 \times 11 \times 9$   $\mathbf{k}$  points is used in the Brillouin zone for geometry optimizations and electronic structure calculations. The lattice parameters of the  $\alpha$ -quartz SiO<sub>2</sub> crystals are chosen to be the same as the experimental values

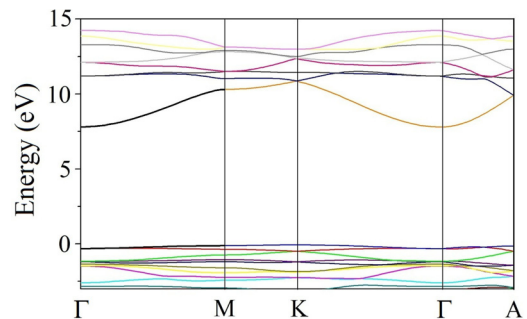


FIG. 9. Band structure of  $p3121$  SiO<sub>2</sub> calculated by high-level HSE06 density functional calculations.

[45,46],  $a = 4.8373 \text{ \AA}$ ,  $b = 4.8373 \text{ \AA}$ ,  $c = 5.3447 \text{ \AA}$  for the  $p3121$  symmetry group and  $a = 4.9137 \text{ \AA}$ ,  $b = 4.9137 \text{ \AA}$ ,  $c = 5.4051 \text{ \AA}$  for the  $p3221$  symmetry group. The band dispersion in Fig. 9 was calculated using the HSE06 hybrid function,

which predicts a band gap of 8.1 eV, close to experiments. The transition dipole moment between the lowest conduction band and the highest valence band was obtained based on the accurate wave functions of the bands.

## APPENDIX B: EXPANSION COEFFICIENTS FOR THE TWO SYMMETRY GROUPS

TABLE I. Expansion coefficients for fitting the lowest conduction band and the highest valence band of  $\text{SiO}_2$  with  $p3121$  symmetry group along the  $\Gamma$ - $M$  direction.

The lowest conduction band					
$\alpha_c(0)$	8.891 57	$\alpha_c(7)$	-0.0026	$\alpha_c(14)$	$5.525 81 \times 10^{-5}$
$\alpha_c(1)$	-1.190 59	$\alpha_c(8)$	0.001 52	$\alpha_c(15)$	$-1.195 29 \times 10^{-4}$
$\alpha_c(2)$	0.132 09	$\alpha_c(9)$	$-9.083 95 \times 10^{-4}$	$\alpha_c(16)$	$7.064 86 \times 10^{-5}$
$\alpha_c(3)$	-0.0486	$\alpha_c(10)$	$5.2744 \times 10^{-4}$	$\alpha_c(17)$	$-2.271 39 \times 10^{-5}$
$\alpha_c(4)$	0.020 03	$\alpha_c(11)$	$-3.227 62 \times 10^{-4}$	$\alpha_c(18)$	$1.821 22 \times 10^{-5}$
$\alpha_c(5)$	-0.009 57	$\alpha_c(12)$	$2.499 48 \times 10^{-4}$	$\alpha_c(19)$	$2.971 38 \times 10^{-7}$
$\alpha_c(6)$	0.004 79	$\alpha_c(13)$	$-1.258 28 \times 10^{-4}$	$\alpha_c(20)$	$-3.261 73 \times 10^{-6}$
The highest valence band					
$\alpha_v(0)$	-0.211 57	$\alpha_v(6)$	$9.118 93 \times 10^{-5}$	$\alpha_v(12)$	$9.792 42 \times 10^{-5}$
$\alpha_v(1)$	-0.094 86	$\alpha_v(7)$	$1.190 69 \times 10^{-4}$	$\alpha_v(13)$	$3.772 27 \times 10^{-5}$
$\alpha_v(2)$	-0.007 85	$\alpha_v(8)$	$1.571 95 \times 10^{-4}$	$\alpha_v(14)$	$9.671 02 \times 10^6$
$\alpha_v(3)$	-0.001 03	$\alpha_v(9)$	$5.105 72 \times 10^{-5}$	$\alpha_v(15)$	$-1.058 62 \times 10^{-4}$
$\alpha_v(4)$	$-3.266 41 \times 10^{-4}$	$\alpha_v(10)$	$5.919 38 \times 10^{-5}$		
$\alpha_v(5)$	$-2.1125 \times 10^{-5}$	$\alpha_v(11)$	$4.622 32 \times 10^{-5}$		

TABLE II. Same as Table I but for  $p3221$  symmetry group.

The lowest conduction band					
$\alpha_c(0)$	8.696 88	$\alpha_c(7)$	-0.002 55	$\alpha_c(14)$	$8.7957 \times 10^{-5}$
$\alpha_c(1)$	-1.139 93	$\alpha_c(8)$	0.0014	$\alpha_c(15)$	$-6.073 \times 10^{-5}$
$\alpha_c(2)$	0.132 36	$\alpha_c(9)$	$-7.181 47 \times 10^{-4}$	$\alpha_c(16)$	$-1.429 26 \times 10^{-5}$
$\alpha_c(3)$	-0.045 73	$\alpha_c(10)$	$4.381 38 \times 10^{-4}$	$\alpha_c(17)$	$-2.958 63 \times 10^{-5}$
$\alpha_c(4)$	0.019 16	$\alpha_c(11)$	$-2.962 92 \times 10^{-4}$	$\alpha_c(18)$	$4.951 89 \times 10^{-5}$
$\alpha_c(5)$	-0.008 93	$\alpha_c(12)$	$2.104 85 \times 10^{-4}$	$\alpha_c(19)$	$-6.567 98 \times 10^6$
$\alpha_c(6)$	0.0046	$\alpha_c(13)$	$-9.922 49 \times 10^{-5}$	$\alpha_c(20)$	$3.6867 \times 10^7$
The highest valence band					
$\alpha_v(0)$	-0.222 94	$\alpha_v(4)$	$9.651 26 \times 10^{-4}$	$\alpha_v(8)$	$-2.827 05 \times 10^{-5}$
$\alpha_v(1)$	-0.122 51	$\alpha_v(5)$	0.001 04	$\alpha_v(9)$	$1.452 84 \times 10^{-4}$
$\alpha_v(2)$	-0.009 19	$\alpha_v(6)$	$5.673 98 \times 10^{-4}$		
$\alpha_v(3)$	$4.675 13 \times 10^{-4}$	$\alpha_v(7)$	$1.979 67 \times 10^{-4}$		

[1] H. G. Muller, P. Agostini, and G. Petite, in *Atoms in Intense Laser Fields*, edited by M. Gavrila (Academic Press, New York, 1992).  
 [2] A. Zavriyev, P. H. Bucksbaum, J. Squier, and F. Saline, *Phys. Rev. Lett.* **70**, 1077 (1993).  
 [3] P. B. Corkum, *Phys. Rev. Lett.* **71**, 1994 (1993).  
 [4] P. B. Corkum and F. Krausz, *Nat. Phys.* **3**, 381 (2007).  
 [5] P. M. Paul, E. S. Toma, P. Breger, G. Mullot, F. Aue, Ph. Balcou, H. G. Muller, and P. Agostini, *Science* **292**, 1689 (2001).  
 [6] M. Hentschel, R. Kienberger, C. Spielmann, G. A. Reider, N. Milosevic, T. Brabec, P. Corkum, U. Heinzmann,

M. Drescher, and F. Krausz, *Nature (London)* **414**, 509 (2001).  
 [7] P. Tzallas, D. Charalambidis, N. A. Papadogiannis, K. Witte, and G. D. Tsakiris, *Nature (London)* **426**, 267 (2003).  
 [8] G. Sansone, E. Benedetti, F. Calegari, C. Vozzi, L. Avaldi, R. Flammini, L. Poletto, P. Villoresi, C. Altucci, R. Velotta, S. Stagira, S. D. Silvestri, and M. Nisoli, *Science* **314**, 443 (2006).  
 [9] E. Goulielmakis, M. Schultze, M. Hofstetter, V. S. Yakovlev, J. Gagnon, M. Uiberacker, A. L. Aquila, E. M. Gullikson, D. T. Attwood, R. Kienberger, F. Krausz, and U. Kleineberg, *Science* **320**, 1614 (2008).

- [10] C. D. Lin, A. T. Le, Z. Chen, T. Morishita, and R. Lucchese, *J. Phys. B: At. Mol. Opt. Phys.* **43**, 122001 (2010).
- [11] S. Ghimire, A. D. DiChiara, E. Sistrunk, P. Agostini, L. F. DiMauro, and D. A. Reis, *Nat. Phys.* **7**, 138 (2011).
- [12] S. Ghimire, A. D. DiChiara, E. Sistrunk, U. B. Szafruga, P. Agostini, L. F. DiMauro, and D. A. Reis, *Phys. Rev. Lett.* **107**, 167407 (2011).
- [13] B. Zaks, R. B. Liu, and M. S. Sherwin, *Nature (London)* **483**, 580 (2012).
- [14] O. Schubert, M. Hohenleutner, F. Langer, B. Urbanek, C. Lange, U. Huttner, D. Golde, T. Meier, M. Kira, S. W. Koch, and R. Huber, *Nat. Photonics* **8**, 119 (2014).
- [15] T. T. Luu, M. Garg, S. Yu. Kruchinin, A. Moulet, M. Th. Hassan, and E. Goulielmakis, *Nature (London)* **521**, 498 (2015).
- [16] G. Vampa, T. J. Hammond, N. Thiré, B. E. Schmidt, F. Légaré, C. R. McDonald, T. Brabec, and P. B. Corkum, *Nature (London)* **522**, 462 (2015).
- [17] G. Vampa, T. J. Hammond, N. Thiré, B. E. Schmidt, F. Légaré, C. R. McDonald, T. Brabec, D. D. Klug, and P. B. Corkum, *Phys. Rev. Lett.* **115**, 193603 (2015).
- [18] M. Hohenleutner, F. Langer, O. Schubert, M. Knorr, U. Huttner, S. W. Koch, M. Kira, and R. Huber, *Nature (London)* **523**, 572 (2015).
- [19] M. Korbman, S. Y. Kruchinin, and V. S. Yakovlev, *New J. Phys.* **15**, 013006 (2013).
- [20] M. Wu, S. Ghimire, D. A. Reis, K. J. Schafer, and M. B. Gaarde, *Phys. Rev. A* **91**, 043839 (2015).
- [21] P. G. Hawkins, M. Y. Ivanov, and V. S. Yakovlev, *Phys. Rev. A* **91**, 013405 (2015).
- [22] Z. Guan, X. X. Zhou, and X. B. Bian, *Phys. Rev. A* **93**, 033852 (2016).
- [23] G. Vampa, C. R. McDonald, G. Orlando, D. D. Klug, P. B. Corkum, and T. Brabec, *Phys. Rev. Lett.* **113**, 073901 (2014).
- [24] C. R. McDonald, G. Vampa, P. B. Corkum, and T. Brabec, *Phys. Rev. A* **92**, 033845 (2015).
- [25] G. Vampa, C. R. McDonald, G. Orlando, P. B. Corkum, and T. Brabec, *Phys. Rev. B* **91**, 064302 (2015).
- [26] D. Golde, T. Meier, and S. W. Koch, *J. Opt. Soc. Am. B* **23**, 2559 (2006).
- [27] D. Golde, T. Meier, and S. W. Koch, *Phys. Rev. B* **77**, 075330 (2008).
- [28] D. Golde, M. Kira, T. Meier, and S. W. Koch, *Phys. Status Solidi B* **248**, 863 (2011).
- [29] P. Földi, M. G. Benedict, and V. S. Yakovlev, *New J. Phys.* **15**, 063019 (2013).
- [30] T. Tamaya, A. Ishikawa, T. Ogawa, and K. Tanaka, *Phys. Rev. Lett.* **116**, 016601 (2016).
- [31] O. D. Mücke, *Phys. Rev. B* **84**, 081202 (2011).
- [32] T. Higuchi, M. I. Stockman, and P. Hommelhoff, *Phys. Rev. Lett.* **113**, 213901 (2014).
- [33] S. Ghimire, G. Ndabashimiye, A. D. DiChiara, E. Sistrunk, M. I. Stockman, P. Agostini, L. F. DiMauro, and D. A. Reis, *J. Phys. B: At. Mol. Opt. Phys.* **47**, 204030 (2014).
- [34] S. Ghimire, A. D. DiChiara, E. Sistrunk, G. Ndabashimiye, U. B. Szafruga, A. Mohammad, P. Agostini, L. F. DiMauro, and D. A. Reis, *Phys. Rev. A* **85**, 043836 (2012).
- [35] A. F. Kemper, B. Moritz, J. K. Freericks, and T. P. Devereaux, *New J. Phys.* **15**, 023003 (2013).
- [36] P. G. Hawkins and M. Y. Ivanov, *Phys. Rev. A* **87**, 063842 (2013).
- [37] Nimrod Moiseyev, *Phys. Rev. A* **91**, 053811 (2015).
- [38] M. S. Wismer, S. Y. Kruchinin, M. Ciappina, M. I. Stockman, and V. S. Yakovlev, *Phys. Rev. Lett.* **116**, 197401 (2016).
- [39] H. Haug and S. W. Koch, *Quantum Theory of the Optical and Electronic Properties of Semiconductors*, 4th ed. (World Scientific, Singapore, 2004).
- [40] X. M. Tong and Sh. I. Chu, *Phys. Rev. A* **61**, 021802(R) (2000).
- [41] X. Chu and Sh. I. Chu, *Phys. Rev. A* **64**, 021403(R) (2001).
- [42] G. Kresse and J. Furthmüller, *Phys. Rev. B* **54**, 11169 (1996).
- [43] John P. Perdew, Kieron Burke, and Matthias Ernzerhof, *Phys. Rev. Lett.* **77**, 3865 (1996).
- [44] G. Kresse and J. Furthmüller, *Comput. Mater. Sci.* **6**, 15 (1996).
- [45] J. D. Jorgensen, *J. Appl. Phys.* **49**, 5473 (1978).
- [46] G. S. Smith and L. E. Alexander, *Acta Crystallogr.* **16**, 462 (1963).